IEEE Access
Multidisciplinary | Rapid Review | Open Access Journal

Received December 12, 2019, accepted December 22, 2019, date of publication January 3, 2020, date of current version January 21, 2020.

Digital Object Identifier 10.1109/ACCESS.2019.2963714

Head CT Image Convolution Feature Segmentation and Morphological Filtering for Densely Matching Points of IoTs

YAO YAO[1], CHANGLIN XIA[2], JITAO LI[1], AND QIONG LI[3]

[1]College of Physics and Telecommunication Engineering, ZhouKou Normal University, Zhoukou 466001, China
[2]College of Information Engineering, Henan Vocational University of Science and Technology, Zhoukou 466001, China
[3]Zhoukou Academy of Agricultural Sciences, Zhoukou 466001, China

Corresponding Author: Qiong Li (15290067998@163.com)

This work was supported in part by the National Natural Science Foundation of China under Grant 11604395 and Grant 11981240358, and in part by the Program for Science and Technology Innovation Talents in Universities of Henan Province under Grant 18HASTIT032.

ABSTRACT With the rapid application of medical imaging technology, the number of medical images is increasing and the form is gradually diversified. The management and retrieval of medical images is an urgent problem to solve. Traditional image matching technology has many limitations due to the complexity of its manual labeling. Therefore, content-based medical image retrieval is a new method to solve this problem. The technique uses the visual attributes contained in the image to establish the feature index of the image, adopts Sparse Connectivity and weight sharing of CNN (Convolutional Neural Network) to obtain the image feature, and then perform feature similarity matching between the query image and the image in the image database, and implement retrieval according to the matching result. The intensive matching based on the Internet of Things has great potential in the application of medical image 3D reconstruction. Compared with the traditional algorithm based on convolution feature segmentation and morphological filtering, the biggest advantage of the proposed algorithm is the computational efficiency, aiming at the same image. The efficiency of dense matching based on the Internet of Things has greatly improved. At the same time, the problem of occlusion, moving objects, rotation, and scaling in multi-view images is well handled. Experiments show that the proposed method can extract more dense and reliable matching points for multi-view images, which is beneficial to the subsequent 3D reconstruction.

INDEX TERMS Image matching, medical image retrieval, sparse connectivity, weight sharing, 3D reconstruction, Internet of Things.

I. INTRODUCTION

In modern medicine, digital imaging, computed tomography imaging, nuclear magnetic resonance spectroscopy, digital blood vessel silhouette, ultrasound, positron emission tomography and many other medical imaging devices produce a variety of forms. Medical imaging plays an indispensable role in medical diagnosis of anatomical examination, pathophysiological information and so on [1]. With the rapid development of computer technology and the increasing advancement of such medical imaging equipment, the number of clinical digital images collected worldwide has exploded in the past decade, and there is an urgent need for a management and proper use of massive medical images [2]. As a result, medical image archiving and communication systems have emerged. In this standard, image data is labeled with letters and digitized index numbers, such as patient name, date of inspection, method of inspection, and the like. In the medical image workflow, it has gradually become the mainstream way of image storage and management [3], [4]. In the image management system, image retrieval is undoubtedly one of the main and even core functions, and it is an important tool for assisting analysis and decision-making. It promptly feeds back the images the doctor needs based on the doctor's request.

Zhang *et al.* [5] proposed a fast imaging method of magnetic resonance compressed sensing based on generating adversarial networks. This method uses GAN to model

The associate editor coordinating the review of this manuscript and approving it for publication was Wei Wei.

low-dimensional manifolds of high-quality MR images. Experimental results show that this method can achieve at least 5 times the scanning acceleration, and the imaging results are significantly better than the traditional compressed sensing algorithm. Liu *et al.* [6] proposed an MR fast imaging method based on a cascaded deep neural network (cascaded DNN). Through multiple alternating processing of CNN and data fidelity terms, the original complex MR image reconstruction problem can be converted into a series of sub-processes for sequential execution, and each sub-process only needs to further optimize the results of the previous sub-process just fine. In order to combine the advantages of traditional iterative reconstruction methods and deep learning methods, Anthimopoulos *et al.* [7] proposed an MR image reconstruction method based on the alternating direction multiplier algorithm-ADMM-Net. The ADMM iterative reconstruction method uses neural networks for re-implementation. The construction of ADMM-Net refers to the classic ADMM, so the reconstruction results of the network are better interpretable. Yang *et al.* [8] proposed using the convolution framework method to explain it theoretically. The convolution framework was originally used to extend the application of the low-rank Hankel matrix theory to inverse problems. Liu *et al.* [9] proposed a deep convolutional frame neural network and proved that the network can achieve perfect reconstruction using a modified linear unit nonlinear activation function. Due to the spatial local characteristics of CNN convolution operations, most of the fast imaging methods based on deep learning currently choose to process in the image domain. However, some image artifacts caused by incompleteness of k-space data are difficult to solve perfectly in the image domain. To solve this problem, Al-Bander *et al.* [10] proposed a fast MR imaging method based on dual-domain deep learning. Corresponding deep CNNs were designed in both the image domain and the frequency domain. Uncollected data is recovered.

This paper chooses to use feature-based methods for dense matching. This paper first briefly introduces some basic concepts and theoretical knowledge that this algorithm needs, and tries to complete the intensive matching. For the problem of inefficiency, it is proposed to use the optimization algorithm to extract feature points to further improve efficiency. Secondly, in order to eliminate mismatch, this paper proposes a densely matched point medical image convolution feature segmentation and morphological filtering for the Internet of Things. This paper also uses the distance constraint, that is, the point pair whose nearest neighbor distance is less than a certain threshold is a more reliable matching point. Finally, the polar line estimation is performed, and the pair of matching points is constrained by the polar line to finally obtain the correct matching point [11]. It combines image processing and analysis, pattern recognition, machine vision, artificial intelligence and human-computer interaction to make deeper use of stored medical image information. It has become one of the research hotspots in the field of medical imaging. Become the mainstream development trend of medical image retrieval.

The rest of our paper was organized as follows. Theory and method were introduced in Section II, such as high precision flexible system parameter calibration, Intensive matching theory and so on. The related application of the proposed system is described in Section III. Experimental results and analysis were discussed in detail in Section IV. Finally, Section V concluded all the work.

II. THEORY AND METHOD

A. HIGH PRECISION FLEXIBLE SYSTEM PARAMETER CALIBRATION

The calibration of the system parameters requires the use of a dedicated calibration phantom. During the parameter calculation process, it is necessary to fit the trajectory of the corresponding position. The required calibration body mold has a relatively accurate size and relative position [12]. For this purpose, the phantom processing requires less than 25 microns. From the aspects of calculation and error, the calibration phantom shown in Figure 1 is designed. The upper and lower circles are precisely positioned in a cylindrical plastic model. In each of the circular shapes, 12 steel balls are equally spaced on 360, and the distribution is the same on the upper and lower circles [13], [14]. Twenty-four steel balls are embedded in a cylindrical PMMA (Polymethyl Methacrylate) material and their position is used as a basis for calculating the parameters.

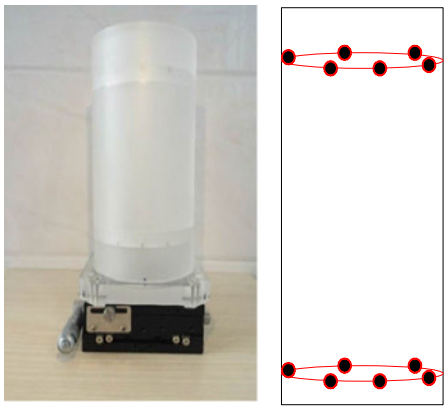

FIGURE 1. System parameter calibration phantom.

In order to ensure that the background around the feature points of the projected picture is not uniform, a plastic cover with the same material as the model is added at each end of the model. To ensure the practicability of the data, the adjacent balls should avoid overlapping when projecting. Put the posture on the hand and adjust the proper posture. Calculate the parameters based on the analysis of the trajectory of the projection point [15]. For better fitting of the elliptical trajectory, a 360-degree rotation projection should have done.

In this paper, by integrating the scanned projection pictures, each point can obtain the corresponding trajectory equation by fitting the ellipse, and analyze the trajectory equation and each feature point to calculate the calculation

of each parameter. At the same time, it is possible to change the pose multiple measurements to reduce the error. Using the existing data, you can calculate all the parameters you need [16]. The following are the calculations of some parameters.

B. INTENSIVE MATCHING THEORY

Dense matching simplifies the algorithm by calculating the integral map, filter approximation, changing the filter size to construct the scale space, etc., taking into account the calculation speed and detection effect, and the detector has considerable repeatability [17]. The feature detection judges whether a point is a feature point according to the determinant value of the Hessian matrix, and the feature point is considered to be a point where the determinant has a maximum value in the scale space. The expression of the Hessian matrix is as follows.

$$h(x,\delta)=\begin{pmatrix} l_{xx}(X,\sigma) & l_{xy}(X,\sigma) \\ l_{xy}(X,\sigma) & l_{yy}(X,\sigma) \end{pmatrix} \tag{1}$$

Among them, $X = (x, y)$ is the point of image I, σ presents the scale space factor, Lxx means the value of the Gaussian second-order partial derivative by xx direction and the convolution of the image I.

$$lxx=\frac{\partial^2}{\partial x^2}g(\sigma)\otimes I \tag{2}$$

The convolution of Gaussian second-order partial derivatives with images is similar to the following. d_{xx} is the discretization of lxx, d_{xy} is the discretization of lxy, d_{yy} is the discretization of lyy.

$$\begin{aligned} l_{xx}(X,\sigma) &\rightarrow d_{xx} \\ l_{xy}(X,\sigma) &\rightarrow d_{xy} \\ l_{yy}(X,\sigma) &\rightarrow d_{yy} \end{aligned} \tag{3}$$

Due to the approximation of the Gaussian convolution kernel, in the determinant calculation, the weight is used to maintain the consistency of the energy before and after the convolution kernel approximation, and the value of the weight determined by the scale [18]. After obtaining the approximate Hessian matrix determinant value, local non-maximal suppression is also required (Non-maxi-Mum suppression), and perform scale space interpolation calculation. In the neighborhood of the scale space, we compute the local maximum of the approximate Hessian matrix determinant for local non-maximal suppression.

The neighborhood includes the corresponding region in the blob response map at three adjacent scales. The blob response maps of different scales are obtained by convolution calculation of the Hessian matrix determinant with box filters of different scales and integral images, as shown in Figure 2.

C. MORPHOLOGICAL FILTERING

Morphological filtering is used to determine the camera pose at three points, and is now widely used in both computer vision and other disciplines. Morphological filtering is very

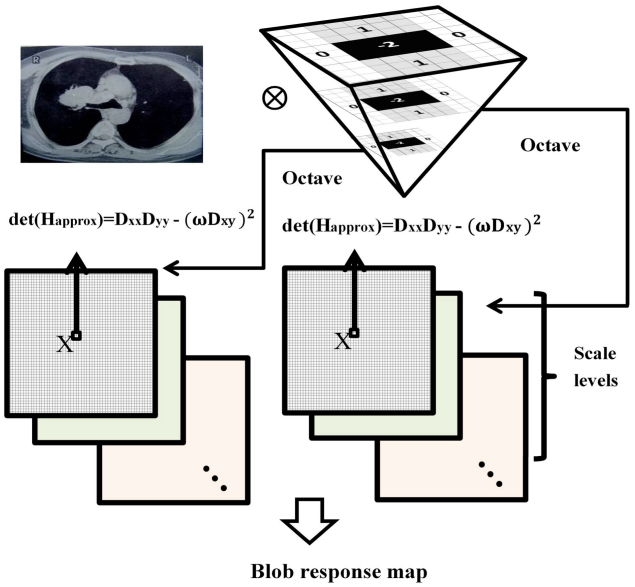

FIGURE 2. Schematic diagram of feature extraction for dense matching.

effective for dealing with large proportions of external points [19], [20]. Here, we will briefly introduce the morphological filtering algorithm. Given the general model M and given measurement data D, the general steps for morphological filtering to estimate model parameters p are as follows.

Determine the solution model, that is, determine the model parameters p, the number of minimum data points n required, and the subset of data points n is called a sample of the model M. A sample is extracted from the data point set D, and an instance of the model is calculated from the sample J, and a set of data points corresponding to the geometric distance threshold is recorded as a consistent set $S(M_p(J))$, which called an instance $M_p(J)$. Figure 2 shows the Morphological filtering for one-dimensional matching. If the number of data points in the consistent set $S(M_p(J))$ is $>$ threshold t, the model is re-estimated and the result is output [21]. If the threshold is t, return to step 2). After K-random sampling, the largest uniform set $S(M_p(J))$ is selected, and the model M is re-estimated by $S(M_p(J))$ and the result is output.

In the matching, the researchers often combined with the morphological filtering algorithm to eliminate the mismatch, and achieved good results [22]. The most typical is to use the morphological filtering algorithm for the estimation of the basic matrix F, to eliminate the mismatch, the main steps as follows.

The feature point sets of the two images are extracted and an initial ''match pair set'' is established. Morphological filtering removes the mismatch pair [23], [24]. The basic matrix F determined by the current sampling, and its consistent set $S(F)$. If the current uniform set $S(F)$ is larger than the original consistent set, keep the current consistent set and the corresponding basic matrix, and delete the original consistent set and the corresponding basic matrix F.

The basic matrix is re-estimated from the largest consistent set (ie, the correct match pair). In order to automatically estimate the basic matrix, it is first necessary to automatically create a ''point correspondence set'' from the two images, that is, to perform automatic matching, which can tolerate a large number of mismatches in the corresponding set, because in the morphological filtering estimation method.

D. MEDICAL INTERNET OF THINGS

After entering the 21st century, the Internet of Things has gradually entered people's field of vision under the background of profound changes in information technology and social production and economic and social development. In addition, in the past 10 years, it has shown a trend of rapid development. In the early concept, the Internet of Things was actually equivalent to RFID (Radio Frequency Identification Devices) technology plus the Internet. Through the information sensing devices such as radio frequency identification, infrared sensors, global positioning systems, laser scanners, etc., the Internet of Things connects any items with the Internet according to the agreed protocol, and exchanges information [25], [26]. The goal is to have all the items connected to the network for easy identification and management. At its core is the application of Internet extensions to all areas of our lives.

At present, the domestic public medical management system is imperfect, the medical cost is high, the channels are small, the coverage is low, the large hospital is overcrowded, and the patient treatment procedures are cumbersome. Wisdom Medical improves the speed of diagnosis and treatment through a fast and improved digital information system, while improving the operational efficiency and regulatory efficiency of the hospital.

(1) Intelligent medical service: electronic medical recording various information such as text, graphics, data, and images generated during medical treatment, storing outpatient and inpatient treatment records [27], [28], facilitating medical treatment, and improving the efficiency of medical staff.

(2) Intelligent medical monitoring: vital signs monitoring—-wearable medical monitoring and alarm system. The multi-parameter acquisition mechanism is used to monitor the patient's blood pressure, pulse, body temperature and blood oxygen content, and the collected signals are transmitted to the medical center through Bluetooth for real-time monitoring.

(3) Medical product management: anti-counterfeiting of drugs—Generally adopt RFID electronic tag identification technology. The manufacturer assigns a unique product electronic code for each batch of drug or even each vial, and attaches the RFID tag to each batch of drug. Throughout the circulation, all producers, wholesalers, retailers and users who may be involved in the drug can use the RFID reader to read the serial number and other information of the drug, and can also access the database according to the drug serial number.

Telemedicine: Telemedicine consultation establishes a new connection between medical experts and patients, enabling patients to receive consultations from remote experts and to provide treatment and care under the guidance of their patients in situ and in the original hospital. It mainly uses the network to communicate voice and high-definition images, and realizes ''face-to-face'' consultation between experts and patients, experts and medical staff.

To a certain extent, it will alleviate the lack of medical service capacity in remote areas and the unbalanced development of medical standards [29]. Medical breakthroughs in geographical limits are conducive to the development of clinical research and improving the level of diagnosis and treatment of small and medium-sized physicians. Medical IoTs was shown in Figure 3.

III. STUDY ON CONVOLUTION FEATURE SEGMENTATION AND MORPHOLOGICAL FILTERING OF DENSELY MATCHING MEDICAL IMAGES

A. FEATURE SEGMENTATION AND EXTRACTION

Due to the huge deformation in the multi-view image, there are also problems such as occlusion, moving objects and inconsistent illumination. Gray-based matching is not suitable. In this paper, we choose to use feature point-based methods for dense matching. The so-called feature points are an important local feature in the image. Compared with other features, the feature points have certain robustness to rotation and changes in illumination conditions. The important grayscale information of the image is not lost; the amount of data participating in the calculation can have greatly reduced.

The number of points extracted by dense matching points is uniform, and more feature points can have extracted whether it is a texture-intensive area or an under-rich area. The extraction feature point has a large gap in both efficiency and effect. Therefore, considering this, the feature segmentation algorithm will have used for feature extraction. Figure 4 is the effect diagram of image feature extraction. For the left and right images, more feature points have extracted. In order to achieve high precision and high efficiency matching, it is very important to select the appropriate feature point description. A good feature descriptor is not only robust to rotation, scaling, and changes in photographic conditions, but also has high efficiency. The most common feature point descriptors have good robustness and have widely used in computer vision and photogrammetry. However, its versatility makes it very inefficient, computationally expensive, and cannot meet actual needs.

B. MULTI-VIEW IMAGE MATCHING IMPLEMENTATION

Multi-view image matching is based on stereo pair matching. Based on the dense matching of stereo pairs, this paper selects three multi-view images for multi-view image matching [30]. Here, we record three images as (v_a, v_b, v_c), selecting two image groups of three images to establish a dense matching of the body image pairs, such as (v_a, v_b), (v_b, v_c), (v_a, v_c).

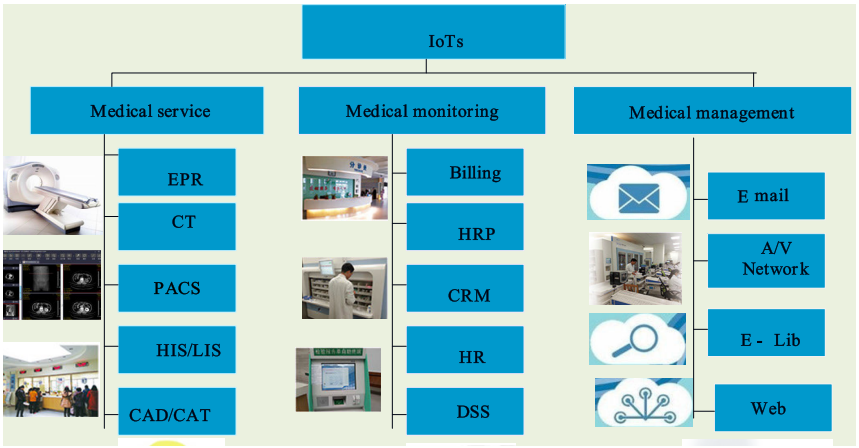

FIGURE 3. Medical IoTs.

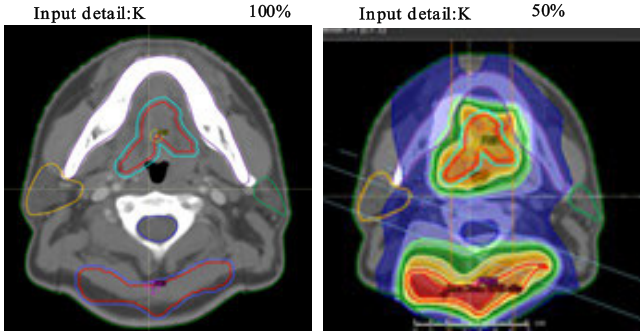

FIGURE 4. Example of image feature extraction.

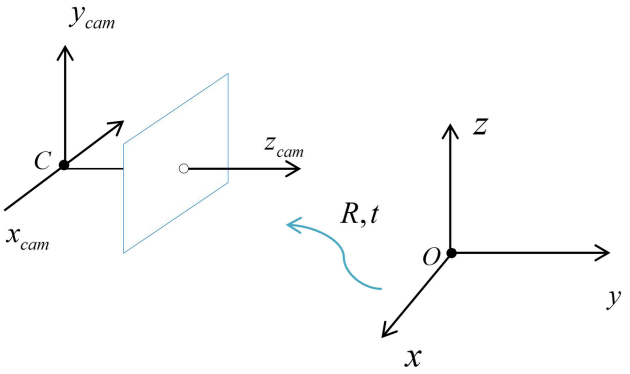

FIGURE 5. Coordinate system conversion diagram.

If there is a matching point pair (f_a, f_b) at (v_a, v_b), there is a matching point pair (f_b, f_c) at (v_b, v_c), then, in the affirmation There is a matching point pair (f_a, f_c) at (v_a, v_c). So that the matching result of the stereo image pair matching (f_a, f_b, f_c) is selected as the matching point of the multi-view image (v_a, v_b, v_c), and the matching of the three images is completed [31].

Based on the dense matching of stereo pairs, this paper selects two images for 3D reconstruction experiments. The process of 3D reconstruction is actually a transformation from point coordinates to object coordinates. There are three coordinate systems involved, such as image point coordinate system, camera coordinate system and object coordinate system. The relationship between the camera coordinate system and the image point coordinate system is shown in Figure 5.

The spatial connection of images is that the local pixel connections are relatively close, while the pixels with far distances are weakly correlated. Therefore, it is not necessary for each neuron to perceive the global image, as long as the local perception is made, then the local layer will be localized. The information is combined to get global information. Implementation with a convolutional layer: local features are extracted from the previous layer by a local convolution filter [32]. This quadratic feature extraction structure reduces feature resolution. The convolution operation is actually extracting a piece of local information, and some statistical characteristics of the local information are the same as other parts, which means that the learned features can also be used in another part. So the same learning characteristics can be used for all positions on the image.

$$X_{cam} = \begin{pmatrix} R & -RC \\ 0 & 1 \end{pmatrix} \begin{bmatrix} x \\ y \\ z \\ 1 \end{bmatrix} = \begin{pmatrix} R & -RC \\ 0 & 1 \end{pmatrix} X \quad (4)$$

where R is the rotation matrix and C is the translation matrix, so the conversion relationship between the image point coordinates and the object coordinates is as follows:

$$\begin{bmatrix} x \\ y \\ 1 \end{bmatrix} = \begin{pmatrix} f_x & 0 & P_X \\ 0 & f_y & p_y \\ 0 & 0 & 1 \end{pmatrix} \begin{pmatrix} R & -RC \\ 0 & 1 \end{pmatrix} \begin{bmatrix} x \\ y \\ z \\ 1 \end{bmatrix} \quad (5)$$

Obviously, an image point coordinate can be listed as two equations. Therefore, the same name image point pair can list 4 equations, and the unknown number is 3. It is a very typical least squares problem. Using the least squares solution,

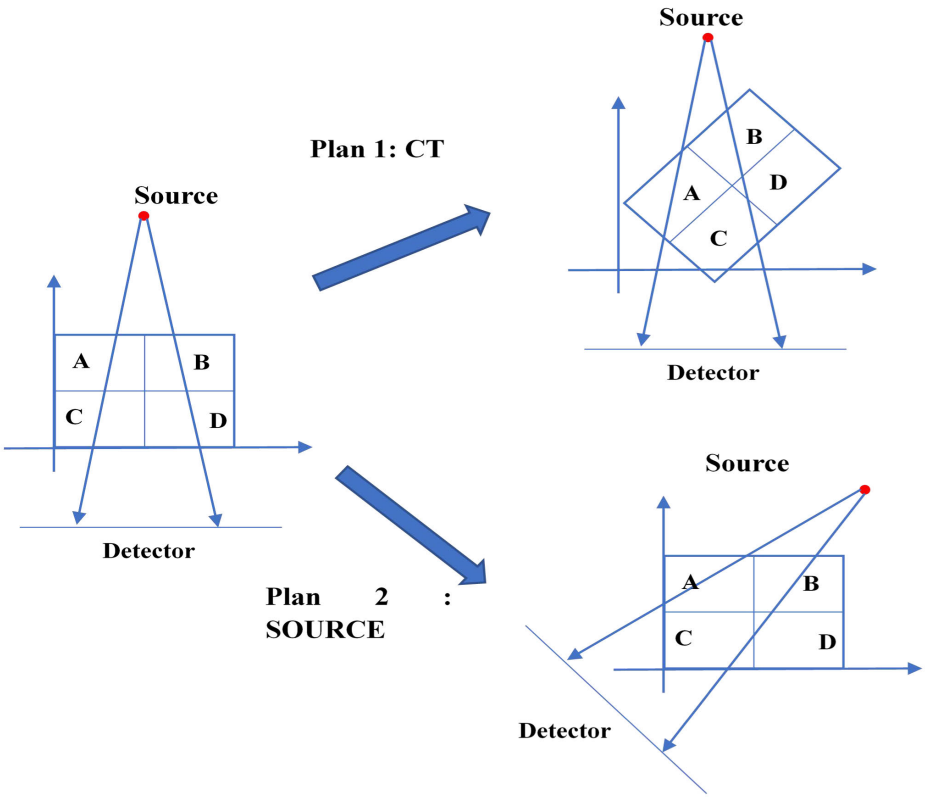

FIGURE 6. Two-dimensional indication of CT positive transformation and inverse transformation of light source and detection panel.

we can get each dimensional point coordinates corresponding to the image points of the same name, that is, the sparse three-dimensional point cloud. Obviously, the sparse three-dimensional point cloud cannot meet the actual needs, and it needs to be interpolated to obtain a more accurate surface model.

C. DRR GENERATION ALGORITHM

In order to calculate the DRR image quickly, the optical path calculation of the corresponding ray source to pixel physical coordinate point in each pixel calculation of the DRR in the Siddon-Jacobs Fast Ray-tracing algorithm is independent of each other. Therefore, it is suitable for parallelization and split calculation of the algorithm. The CT is placed in the space coordinate system with the coordinate axis as the edge, and the CT center is the intersection of the two virtual ray center-lines [33]. The distance from the source to the intersection of the rays is SAD, and the distance from the source to the plane coordinate system is SID. The intersection of the line of the ray source and the CT center point and the 2D plane is taken as the center point of the DRR image, and the spatial physical coordinates of all DRR pixel points are calculated according to the preset DRR size and the physical size of the pixel. The Grid and Block dimensions of CUDA are set according to the DRR size, so that the calculation of each DRR pixel is handled by one thread, and the DRR generation is fully parallelized. When the CT data is transformed in the space coordinate system, the CT data of the new position needs to be interpolated to calculate each voxel value, which is very time consuming [34]. The inverse of the light source point and the panel causes the voxel that each optical path passes to be equivalent to the interpolation result. The two-dimensional schematic diagram is shown in Figure 6. Under the positive transformation of the scheme 1 and the inverse transformation of the scheme 2, the voxels corresponding to the optical path are completely identical. The spatial transformation and interpolation of the complexity O(n3) is reduced to the spatial transformation of the O(n2) plane coordinate system, and no interpolation is needed to avoid the introduction of errors in the continuous transformation of the CT value.

D. DENSE MATCHING POINT MEDICAL IMAGE REGISTRATION PROCESS

1) 2D-2D APPROXIMATE RIGID BODY REGISTRATION

According to the relationship between the space coordinate system and the plane coordinate system established in Section 1, it can be known that 2D-2D rigid body registration can be performed on two pairs of DRR-X ray images in two orthogonal plane coordinate systems to calculate the space coordinates. Tx, Ty, Tz, Rx, Ry in the rigid body transformation parameters. In fact, the difference between the corresponding parameter Rz when generating the X-ray image and

the DRR is generated, and the change of the spatial parameter in the DRR generation is not a factor that is expressed independently on a certain plane. For example, the rotation Rx along the X-axis direction appears as a rotation r2 in the plane coordinate system o2, but brings a predictable simple affine deformation (the y1 axis deflation) on the DRR image contour on the plane coordinate system o1 [35]. At the same time, it exhibits a highly nonlinear effect on pixel values. This is because the optical path between the ray source and the DRR pixel coordinates after the rotation has undergone a slight change in the path length of the different CT voxels or in the same voxel. In order to perform 2D-2D registration in the presence of small non-rigid body differences, a weighted mean similarity measure $Metric_{LWM}$ is designed. For two images I_1, I_2 of size N^*M, the metric $Metric_{LWM}$ is calculated as follows:

For image I, binarization with a mean threshold is performed, and the i-th row and j-column pixels of the binarization result I' are as follows.

$$I'(i,j) = \begin{cases} 1, & I(i,j) \geq Th \\ 0, & I(i,j) < Th, \end{cases}$$
$$Th = \frac{1}{N^*M} \sum_{i,j}^{N,M} I(i,j) \tag{6}$$

For the two binarized images I'_1, I'_2, the i-th row and j-column element $M(i,j)$ of the residual weighted mean matrix M:

$$M(i,j) = \sum_{\substack{p=i-n, \\ q=j-m}}^{\substack{i+n, \\ j+m}} \beta \frac{\left|I'_1(p,q) - I'_2(p,q)\right|}{\beta + \alpha} \tag{7}$$

The parameter m, n is the length and width of the rectangular area of the local pixel block, which α, β is calculated by the following formula:

$$\beta = \begin{cases} 1, & if\ i \neq p, j \neq q \\ \alpha, & if\ i = p, j = q, \end{cases}$$
$$\alpha = (2n+1)(2m+1) - 1 \tag{8}$$

According to further calculation of similarity $Metric_{LWM}$:

$$Metric_{LWM} = 1 - \frac{\sum_{i=1,j=1}^{N,M} M(i,j)}{N^*M} \tag{9}$$

Under this metric, the X-DRR image pairs on the 2D plane can be approximated by rigid body registration, and the transformation results on the plane reflect the spatial transformation to some extent [36]. It can be used to guide the inverse transformation of the light source and panel in the second section to speed up the iteration. The 2D-2D approximate rigid body registration process is shown in Figure 7.

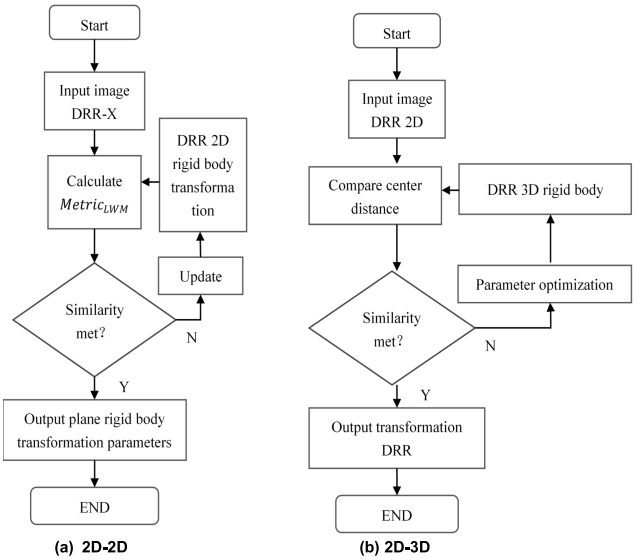

FIGURE 7. The image matching based on 2D and 3D.

2) 2D-3D APPROXIMATE RIGID BODY REGISTRATION

According to the 2D-2D approximate rigid body registration algorithm, the 2D-2D registration results of two pairs of DRR-X ray images are calculated and updated by the formula (1)∼ formula (3), and the corresponding spatial rigid body transformation parameters Tx, Ty, Tz, Rx and Ry. For the ray source points S1 and S2 in the space coordinate system and the corresponding two plane coordinate systems, the spatial rigid body transformation with parameters -Tx, -Ty, -Tz, -Rx, -Ry, -Rz is performed by the new spatial coordinate system. The plane coordinate system generates a new pair of DRR images and calculates the NCC (Normalized Cross Correlation) metric between the DRR-X ray image pairs.

For two images I_1, I_2 of the same size N^*M, the metric $NCC(I_1, I_2)$ is calculated as follows:

$$NCC(I_1, I_2) = \frac{Cvar(I_1, I_2)}{\sqrt{Var(I_1)^* Var(I_2)}} \tag{10}$$

The calculation $Cvar(I_1, I_2)$ is as follows:

$$Cvar(I_1, I_2) = \frac{\sum_{i=1,j=1}^{N,M} \left(\left(I_1(i,j) - \overline{I_1}\right)^* \left(I_2(i,j) - \overline{I_2}\right) \right)}{N^*M}$$

For image-I, the calculation $S(M_p(J))$ is as follows:

$$Var(I) = \frac{\sum_{i=1,j=1}^{N,M} (I(i,j) - \bar{I})^2}{N^*M} \tag{11}$$

According to the value of the NCC metric, the coordinate rotation search is performed on the six rigid body transformation dimensions of the spatial coordinate system. The spatial rigid body transformation parameters are updated by the 2D-2D registration result of the search. The main steps are described as follows. Read CT and X-ray image data, establish a coordinate system, and assign physical coordinates to CT voxels and DRR pixels.

According to the current parameters Tx, Ty, Tz, Rx, Ry, Rz, a pair of orthogonal DRR images are generated, and 2D-2D registration is performed respectively with the corresponding X-ray images. The initial parameters of the 2D-2D registration are from the orthogonal decomposition of the spatial rigid body transformation parameters, and the Tx, Ty, Tz, Rx, Ry are updated by the registration results between the two pairs of DRR-X-ray images.

According to the updated parameters in 2), the GPU accelerates again to generate a new pair of DRR images. Calculate the NCC metric between the DRR and the corresponding X-ray image, and perform a round search to update one of Tx, Ty, Tz, Rx, Ry, Rz.

Repeat 2) to 3) until the increment of the NCC metric in 3) between the iterations is less than the threshold. The current parameters Tx, Ty, Tz, Rx, Ry, Rz and their corresponding DRR images are output.

The 2D-2D registration result is more reliable because the Rz parameter in the iteration 3) search result is closer to the target value.

IV. EXPERIMENTS AND RESULTS

The dense matching point medical image for the Internet of Things is a technology that reconstructs a two-dimensional medical image sequence into a three-dimensional stereoscopic image through computer visualization technology and intuitively displays it on the screen, providing users with a series of interactive functions. In medical diagnosis, because it can provide real 3D medical images, doctors can analyze the lesion areas and other tissues and organs of interest from multiple angles and levels. Greatly it improved the accuracy of doctors' diagnosis, which can provide strong support for the diagnosis and treatment of doctors.

A. DATABASE RUNTIME ENVIRONMENT

With the rapid application of IoTs, IoT technology is increasingly used in medical imaging. The IoT application is the collection of massive medical images. The combination of intensive matching point medical images and feature segmentation technology enables the Internet of Things to further integrate into people's production and life. In this paper, IoT technology is used to design acquisition equipment based on dense matching point medical images, and CT images are collected as research databases. Figure 8 is a design diagram of a medical image based on an intensive matching point of the Internet of Things.

B. PROGRAM RUNNING

After pressing the exposure button, the image is immediately exposed, and the received image quality is very poor. The reason is that the Acquire Prepare function called before the 2D tablet acquisition requires <700ms, and the Acquisition Trigger function starts to <125ms when the "Exposure Event On" event occurs. Therefore, it is speculated that the delay in "Workstations" is changed to 650ms in the EMD software. Figure 9 shows the exposure state switch.

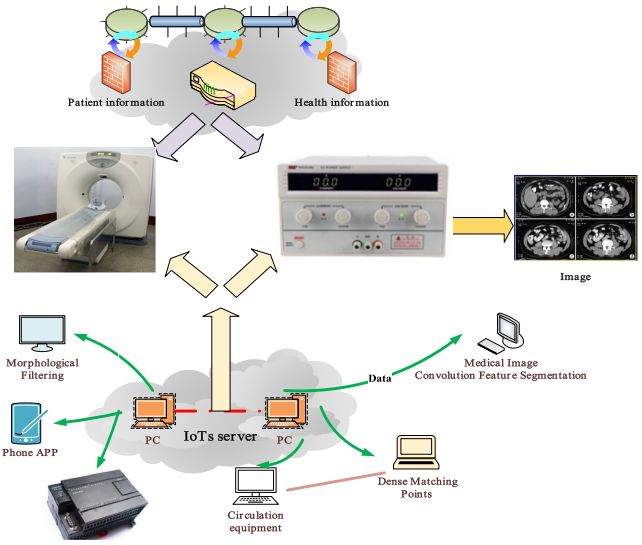

FIGURE 8. Medical image architecture diagram based on IoTs.

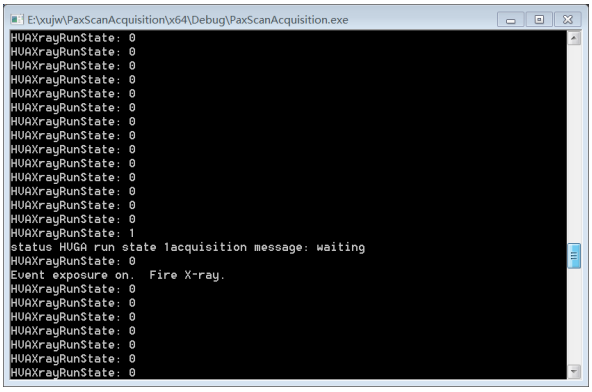

FIGURE 9. The Exposure state switching.

The experimental data is the head image after the head field segmentation. The front image is the head cancer image, the normal image of the head, the image of the heads with enhanced texture, and the remaining image is the bronchitis image. Based on the head phantom localization imaging technology that has been compiled and run, this paper uses the dense matching point method to perform multi-point calibration of head images that have been segmented by the head field, as shown in Figure 10.

The experiment selected a CT picture of a common human head. Figure 11 is a reference picture, which select from *DeepLesion* Imaging Database. The treatment of these differences is the focus and difficulty of our entire image registration work.

C. SELECTION OF EXPERIMENTAL PARAMETERS

The ratio of the cross-sectional area of the image size to the volume data size changes, and the pixel spacing that generates the DRR needs to be re-adjusted to generate a DRR image of a suitable size and good filling effect (avoiding a large

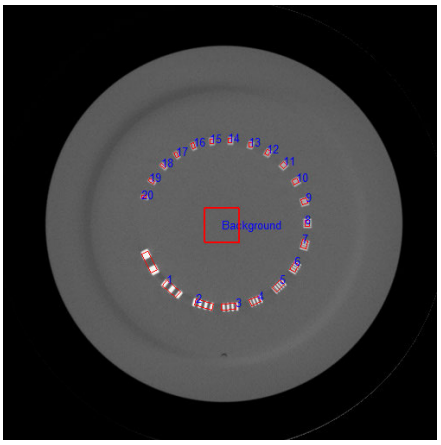

FIGURE 10. The Phantom calibration position map.

FIGURE 11. The CT Reference map.

FIGURE 12. DRR image of a suitable size and good filling.

(Rotate)

(Translate)

FIGURE 13. Two method of image matching.

black background that is meaningless) for registration. The following two are in the 1:2 ratio of the original sad and sid and the 1:3 under the current mechanical structure, the pixel spacing is 1mm*1mm, and the image size is 256*256 when the DRR image.

Change the pixel spacing of 0.5mm*0.5mm to produce an image whose size is almost the same as the original ratio, which is more suitable for registration. The image shows the image generated under the current mechanical structure parameters in Figure 12.

Rotate -15° 20° 2° along XYZ, translate -15mm 10mm 5mm to create two angled 75° DRR images. The upper picture shows the 45-degree detection panel image, the picture below is -30 degree in Figure 13.

D. FILTER PROCESSING

Due to the quality problem of the image to be processed, the image to be processed should be pre-processed before being easily extracted. The specific operation is as follows. When the image is acquired, the image is blurred due to the relative motion between the scene and the camera. Among them, the problem of restoration of blurred images caused by uniform linear motion is more general and universal. The variable speed and non-linear motion can be regarded as the result of uniform and linear motion under certain conditions [7].

The model of image blur caused by uniform linear motion in the horizontal direction and the approximate formula for recovery are expressed by the following

TABLE 1. Experimental results of dense matching points.

Initial position	Output rotation （X_Y_Z，degree）			Output displacement （X_Y_Z，mm）			Time
error along the X	-15.006	20	2	-15	10	5	7m21s
5° error along the Y	-15	19.944	2	-15	10	5	7m17s
5° error along the Z	-14.961	20.014	2.038	-15.931	10	5.009	14m29s
5° error along the XYZ	-15.047	19.923	2.036	-15.032	10.03	5.007	16m11s
5mm error along the X	-15.007	20.130	2.128	-15.974	10.029	4.973	16m8s
5mm error along the Y	-15.045	19.840	1.895	-15.011	10.008	5.022	17m11s
5mm error along the Z	-15.106	20.065	2.036	-15.026	10.005	5.041	13m49s
5mm error along the XYZ	-14.974	20.075	1.890	-15.066	10.034	5.024	22m2s
5mm & 5°error along the XYZ	-15.091	19.99	1.972	-15.048	10.056	5.084	20m14s

two equations.

$$g(x,y) = \int_0^T f\left[(x - \frac{at}{T}), y\right]dt \tag{12}$$

$$f(x,y) \approx A - mg'\left[(x - ma), y\right] + \sum_{k=0}^{m} g'\left[(x - ka), y\right]$$

$$0 \le xy \le L \tag{13}$$

where a is the total displacement and T is the total exercise time.

In order to ensure that the global optimal solution can guarantee the registration accuracy in the optimization, the registration optimization needs to be divided into two parts: initialization and precise registration. The template matching method is used to match the X-ray image with a series of pre-generated DRR images to select the DRR with the highest similarity. The generation parameter of the DRR (rotational translation of the 3D volume data, etc.) is taken as the initialization value of the next step. In the template matching process, the multi-resolution pyramid matching is adopted, and the image information is reduced and reduced according to a certain rule. From the top layer, each layer is calculated and a part of the image with a large difference is discarded, and the remaining images are entered into the next layer to continue the calculation. The image that best matches the X-ray image is filtered out until the last layer. Compared with the way of calculating the X-ray and DRR matching degree by traversing directly on the original image, this strategy will match the calculation of some images in each layer, but the image size is smaller in the layer with higher pyramid. The DRR images with large differences are eliminated as early as possible, and the number of remaining DRR images in the lower layer is much reduced. Table 1 showed this method can accelerate the search for the best matching DRR and complete the initialization parameters.

Registration accuracy is very accurate in translation, with errors at the sub-pixel level. There is almost no difference in the resulting registration results. The visible accuracy can fully meet the requirements of the index and has greatly shortened in time. However, the 2D images used in this experiment are not real X-ray images and may differ when using real X-ray images. The result of the above filtered image is shown in Figure 14.

FIGURE 14. Results of image matching and filtering.

A densely matched point medical image convolution feature segmentation and morphological filtering system for the Internet of Things, enabling user registration, patient information import, planning CT data import, patient scanning, 3D reconstruction of 2D projection data, and image registration with planned CT images and the function of patient placement error output. The software uses a software interface and system function layered decoupling design to facilitate subsequent function expansion. The key technologies involved in the latest software release include image system calibration, 3D reconstruction, and image registration. System calibration is used to verify the geometric relationship between the X-ray imaging source, the phantom, and the flat panel detector, providing high precision and geometric parameters for 3D reconstruction after multi-angle rotational scanning imaging. The 3D reconstruction uses a multi-point matching algorithm with a pure planar circular trajectory,

which can have better reconstruction quality near the mid-plane. Image registration is based on the reconstructed 3D volume data and the loaded plan CT for 3D-3D registration to obtain the patient placement error.

V. CONCLUSION

Image registration is a key technology in the fields of remote sensing image processing, target recognition, image reconstruction, robot vision, etc. It is the basis of multi-sensor image fusion. Image registration is required in many fields such as military, remote sensing, medicine, and computer vision. The actual application process with IOT may be different, but the key factors are similar. This paper takes medical imaging as the research object, and realizes computer-aided diagnosis through image registration, which is helpful for doctors to diagnose the patient's condition. The main work includes the following sections. The research background and significance of the subject are described in detail. The analysis of the research status of medical image retrieval based on the Internet of Things and dense registration points, including the introduction of key technologies for feature segmentation, based on the principle of content image registration and its frame structure. It also introduces the application in the medical field, and gives a framework diagram of medical image matching points based on the Internet of Things. According to the research status of texture features, a variety of methods for extracting medical image features based on statistics and transformation are introduced. The head image is described in detail, and the image is used as experimental data in this paper. The automatic segmentation method of a digital head image region is used to segment the feature, and the segmented image is quickly registered.

REFERENCES

[1] T. Wang, H. Feng, S. Li, and Y. Yang, "Design and implementation of automated QA software for cone beam CT image," *Chin. J. Med. Instrum.*, vol. 43, no. 1, pp. 25–28, 2019.

[2] L. Cheng, Y.-K. Zhang, Y. Song, C. Li, and D.-S. Guo, "Low–dose CT image restoration based on adaptive prior feature matching and nonlocal means," *Int. J. Image Graph.*, vol. 19, no. 3, Jul. 2019, Art. no. 1950017.

[3] G. Litjens, T. Kooi, B. E. Bejnordi, A. A. A. Setio, F. Ciompi, M. Ghafoorian, J. A. Van Der Laak, B. Van Ginneken, and C. I. Sánchez, "A survey on deep learning in medical image analysis," *Med. Image Anal.*, vol. 42, pp. 60–88, Dec. 2017.

[4] Q. Yan, D. Gong, and Y. Zhang, "Two–stream convolutional networks for blind image quality assessment," *IEEE Trans. Image Process.*, vol. 28, no. 5, pp. 2200–2211, May 2019.

[5] J. Zhang, Y. Xia, H. Zeng, and Y. Zhang, "NODULe: Combining constrained multi-scale LoG filters with densely dilated 3D deep convolutional neural network for pulmonary nodule detection," *Neurocomputing*, vol. 317, pp. 159–167, Nov. 2018.

[6] Z.-F. Liu, Y.-Z. Zhang, P.-Z. Liu, Y. Zhang, Y.-M. Luo, Y.-Z. Du, Y. Peng, and P. Li, "Retinal vessel segmentation using densely connected convolution neural network with colorful fundus images," *J. Med. Imaging Health Informat.*, vol. 8, no. 6, pp. 1300–1307, Aug. 2018.

[7] M. Anthimopoulos, S. Christodoulidis, L. Ebner, A. Christe, and S. Mougiakakou, "Head pattern classification for interstitial head diseases using a deep convolutional neural network," *IEEE Morpholog. Filtering Med. Imag.*, vol. 35, no. 5, pp. 1207–1216, May 2016.

[8] D. Yang, M. Ren, and B. Xu, "Retinal blood vessel segmentation with improved convolutional neural networks," *J. Med. Imag. Health Inf.*, vol. 9, no. 6, pp. 1112–1118, Aug. 2019.

[9] S. Liu, D. Xu, S. K. Zhou, O. Pauly, S. Grbic, T. Mertelmeier, J. Wicklein, A. Jerebko, W. Cai, and D. Comaniciu, "3D anisotropic hybrid network: Transferring convolutional features from 2D images to 3D anisotropic volumes," in *Proc. Int. Conf. Med. Image Comput. Comput.-Assist. Intervent.* Cham, Switzerland: Springer, Sep. 2018, pp. 851–858.

[10] B. Al-Bander, B. Williams, W. Al-Nuaimy, M. Al-Taee, H. Pratt, and Y. Zheng, "Dense fully convolutional segmentation of the optic disc and cup in colour fundus for glaucoma diagnosis," *Symmetry*, vol. 10, no. 4, p. 87, Mar. 2018.

[11] I. B. De Medeiros, M. A. Soares Machado, W. J. Damasceno, A. M. Caldeira, R. C. Dos Santos, and J. B. Da Silva Filho, "A fuzzy inference system to support medical diagnosis in real time," *Procedia Comput. Sci.*, vol. 122, pp. 167–173, Jan. 2017.

[12] R. Yao, S. Liao, X. Chen, G. Tang, G. Wang, and F. Zheng, "Effects of ZnO and NiO on material properties of microwave absorptive glass-ceramic tile derived from iron ore tailings," *Ceram. Int.*, vol. 42, no. 7, pp. 8179–8189, May 2016.

[13] P. Zheng, Y. Wang, X. Xu, and S. Q. Xie, "A weighted rough set based fuzzy axiomatic design approach for the selection of AM processes," *Int. J. Adv. Manuf. Technol.*, vol. 91, nos. 5–8, pp. 1977–1990, Jul. 2017.

[14] C.-M. Pun, X.-C. Yuan, and X.-L. Bi, "Image forgery detection using adaptive oversegmentation and feature point matching," *IEEE Trans. Inf. Forensics Security*, vol. 10, no. 8, pp. 1705–1716, Aug. 2015.

[15] S. R. Hashemi, S. S. Mohseni Salehi, D. Erdogmus, S. P. Prabhu, S. K. Warfield, and A. Gholipour, "Asymmetric loss functions and deep densely–connected networks for highly–imbalanced medical image segmentation: Application to multiple sclerosis lesion detection," *IEEE Access*, vol. 7, pp. 1721–1735, 2019.

[16] S. Hao, L. Yang, and Y. Shi, "Data-driven car-following model based on rough set theory," *IET Intell. Transp. Syst.*, vol. 12, no. 1, pp. 49–57, Feb. 2018.

[17] D. Das and S. Mukhopadhyay, "Fingerprint image segmentation using block–based statistics and morphological filtering," *Arabian J. Sci. Eng.*, vol. 40, no. 11, pp. 3161–3171, Nov. 2015.

[18] X. Wang, L. Yao, H. Wen, and J. Zhao, "Wolfberry image segmentation based on morphological multi-scale reconstruction and concave points matching," *Trans. Chin. Soc. Agricult. Eng.*, vol. 34, no. 2, pp. 212–218, 2018.

[19] H. Li, L. Li, and J. Zhang, "Multi-focus image fusion based on sparse feature matrix decomposition and morphological filtering," *Opt. Commun.*, vol. 342, pp. 1–11, May 2015.

[20] H. Li, "Deep learning for natural language processing: Advantages and challenges," *Nat. Sci. Rev.*, vol. 5, no. 1, pp. 24–26, Jan. 2018.

[21] S. Pouyanfar and S.-C. Chen, "Automatic video event detection for imbalance data using enhanced ensemble deep learning," *Int. J. Semantic Comput.*, vol. 11, no. 1, pp. 85–109, Mar. 2017.

[22] H. Venkateswara, S. Chakraborty, and S. Panchanathan, "Deep–learning systems for domain adaptation in computer vision: Learning transferable feature representations," *IEEE Signal Process. Mag.*, vol. 34, no. 6, pp. 117–129, Nov. 2017.

[23] X. Gao, F. Li, and K. Wan, "Accelerated learning for restricted Boltzmann machine with a novel momentum algorithm," *Chin. J. Electron.*, vol. 27, no. 3, pp. 483–487, May 2018.

[24] Harsiti, T. A. Munandar, A. Suhendar, A. G. Abdullah, and D. Rohendi, "Contrast enhancement for satellite image segmentation with fuzzy cluster means using morphological filtering," *IOP Conf. Ser., Mater. Sci. Eng.*, vol. 128, Apr. 2016, Art. no. 012054.

[25] A. M. Sheri, A. Rafique, W. Pedrycz, and M. Jeon, "Contrastive divergence for memristor-based restricted Boltzmann machine," *Eng. Appl. Artif. Intell.*, vol. 37, pp. 336–342, Jan. 2015.

[26] Z. Zhou, W. Wu, S. Wu, P.-H. Tsui, C.-C. Lin, L. Zhang, and T. Wang, "Semi-automatic breast ultrasound image segmentation based on mean shift and graph cuts," *Ultrason. Imag.*, vol. 36, no. 4, pp. 256–276, Oct. 2014.

[27] J.-H. Lee, D.-H. Kim, S.-N. Jeong, and S.-H. Choi, "Diagnosis and prediction of periodontally compromised teeth using a deep learning-based convolutional neural network algorithm," *J. Periodontal Implant Sci.*, vol. 48, no. 2, pp. 114–123, 2018.

[28] A. Y. Rubis, M. A. Lebedev, Y. V. Vizilter, and O. V. Vygolov, "Morphological image filtering based on guided contrasting," *Comput. Opt.*, vol. 40, no. 1, pp. 73–79, Sep. 2016.

[29] Z. Song, Y. Liu, R. Song, Z. Chen, J. Yang, C. Zhang, and Q. Jiang, "A sparsity-based stochastic pooling mechanism for deep convolutional neural networks," *Neural Netw.*, vol. 105, pp. 340–345, Sep. 2018.

[30] Y. Guo, Q. Liu, G. Liu, and C. Huang, "Individual tree crown extraction of high resolution image based on marker-controlled watershed segmentation method," *J. Geo-Inf. Sci.*, vol. 18, no. 9, pp. 1259–1266, 2016.
[31] B. Shi, X. Bai, and C. Yao, "Script identification in the wild via discriminative convolutional neural network," *Pattern Recognit.*, vol. 52, pp. 448–458, Apr. 2016.
[32] Z. Wu, Y. Huang, L. Wang, X. Wang, and T. Tan, "A comprehensive study on cross–view gait based human identification with deep CNNs," *IEEE Trans. Pattern Anal. Mach. Intell.*, vol. 39, no. 2, pp. 209–226, Feb. 2017.
[33] C. Shan, B. Huang, and M. Li, "Binary morphological filtering of dominant scattering area residues for SAR target recognition," *Comput. Intell. Neurosci.*, vol. 2018, pp. 1–15, Dec. 2018.
[34] Y. Xu, T. Geraud, and L. Najman, "Connected filtering on tree–based shape–spaces," *IEEE Trans. Pattern Anal. Mach. Intell.*, vol. 38, no. 6, pp. 1126–1140, Jun. 2016.
[35] J. Wang, X. Li, Y. Zhang, and X. Zhang, "Adaptive decomposition method for multi-modal medical image fusion," *IET Image Process.*, vol. 12, no. 8, pp. 1403–1412, Aug. 2018.
[36] B. Song, D.-K. Baik, and S. Zhou, "Human eye location algorithm based on multi-scale self-quotient image and morphological filtering for multimedia big data," *Multimed. Tools Appl.*, vol. 77, no. 8, pp. 10063–10075, Apr. 2018.

YAO YAO received the master's degree from Chongqing University, in 2009. He is currently a Lecturer with the College of Physics and Telecommunication Engineering, ZhouKou Normal University. His research interest includes deep learning.

CHANGLIN XIA received the bachelor's degree from Henan Polytechnic University, in 2007. He is currently a Lecturer with the College of Information Engineering, Henan Vocational University of Science and Technology. His research interests include machine learning and image processing.

JITAO LI received the Ph.D. degree from Southeast University, in 2015. He is currently an Associate Professor with the College of Physics and Telecommunication Engineering, ZhouKou Normal University. His research interest includes deep learning.

QIONG LI received the master's degree from Xinjiang Agricultural University, in 2012. He is currently an Assistant Researcher with the Zhoukou Academy of Agricultural Sciences. His research interest includes bioinformatics.